

Identifying Microstructural Changes in Diffusion MRI; How to Break Parameter Degeneracy

Hossein Rafipoor¹, Ying-Qiu Zheng¹, Ludovica Griffanti^{1,2}, Saad Jbabdi¹, and Michiel Cottaar¹

¹Wellcome Centre for Integrative Neuroimaging, FMRIB, Nuffield Department of Clinical
Neurosciences, Oxford, UK

²Wellcome Centre for Integrative Neuroimaging, Oxford Centre for Human Brain Activity,
Department of Psychiatry, University of Oxford, Oxford, UK

ABSTRACT

Biophysical models that attempt to infer real-world quantities from data usually have many free parameters. This over-parameterisation can result in degeneracies in model inversion and render parameter estimation ill-posed. However, often, we are not interested in estimating the parameters *per se*, but rather in identifying changes in parameters between experimental conditions (e.g. patients vs controls). Here we present a Bayesian framework to make inference on changes in the parameters of biophysical models even when model inversion is degenerate, which we refer to as Bayesian EstimatioN of CHange (BENCH).

We infer the parameter changes in two steps; First, we train models that can estimate the pattern of change in the measurements given any hypothetical change in the parameters using simulations. Next, for any pair of real data sets, we use these pre-trained models to estimate the probability that an observed difference in the data can be explained by each model of change.

The approach is general and particularly useful for biophysical models with parameter degeneracies. In this paper, we apply the approach in the context of microstructural modelling of diffusion MRI data, where the models are usually over-parameterised and not invertible without injecting strong assumptions. Using simulations, we show that in the context of the standard

24 model for diffusion our approach is able to identify changes in microstructural parameters from
25 multi-shell diffusion MRI data. We also apply our approach to a subset of subjects from the
26 UK-Biobank Imaging to identify the dominant standard model parameter change in areas of white
27 matter hyperintensities.

28 INTRODUCTION

29 Modelling diffusion MRI (dMRI) data comes in two flavours. Phenomenological models, such
30 as diffusion tensor imaging (DTI) (Basser et al. 1994) and DKI (Jensen et al. 2005)) attempt to
31 capture the structure of the data, while (bio)physical models such as the standard model (Novikov
32 et al. 2019a), NODDI (Zhang et al. 2012), Ball and Rackets (Sotiropoulos et al. 2012) and AxCaliber
33 (Assaf et al. 2008)) attempt to infer properties of the tissue microstructure given the data. This active
34 field of research relies on the inversion of biophysical forward models, but it is also notoriously
35 difficult to overcome model degeneracies (Jelescu et al. 2016). To resolve these degeneracies,
36 the conventional approach is to constrain a subset of the parameters and only make inferences on
37 the remaining parameters (Zhang et al. 2012). However, the validity of the extra assumptions,
38 specifically under different experimental conditions is unclear. As a result, not only is there a
39 limit to the number of microstructural parameters that can be estimated, but the reliability of the
40 estimated parameters can also be questionable (Jelescu et al. 2016; Reisert et al. 2017; Lampinen
41 et al. 2019).

42 However, in many real-world applications, the model parameters may not be of direct interest.
43 Rather, we are often interested in the “change” in the parameters under different experimental
44 conditions. For example, to study mechanisms underlying a disease one would normally compare
45 the parameter estimates of biophysical models between patient and control groups, with little
46 attention paid to the actual parameter estimates. However, the parameter estimation is only tractable
47 when the model of interest is invertible given the data. This limits one to simple biophysical models
48 or requires injection of prior assumptions.

49 In this work, we show that we can make precise inferences on the change in model parameters
50 even in complex degenerate models. We argue that, using a sparsity assumption on the pattern

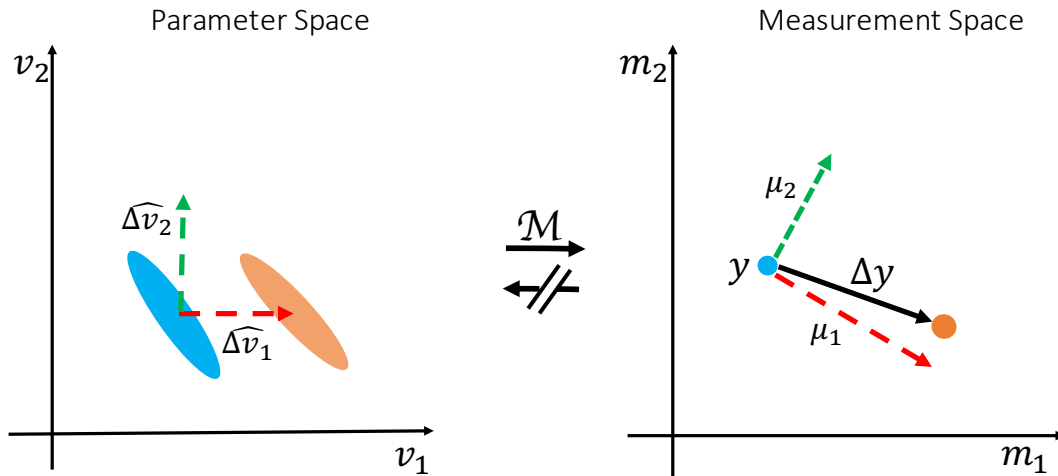


Figure 1. Illustration of the inversion-free inference on change (BENCH). Consider a toy model with two parameters and two measurements $\mathcal{M}(v_1, v_2) = [m_1, m_2]$. Each oval in the parameter space (left) corresponds to a single point in the measurement space (right) with the same color; meaning that there is a one to many mapping from measurements to parameters (i.e., the model is degenerate). Despite the degeneracies we are able to estimate which of the parameters best explains the change in the measurements. We do so by comparing the observed change (Δy) with the expected change in the measurements (μ_1, μ_2) as a result of each hypothesised pattern of change ($\Delta \hat{v}_1, \Delta \hat{v}_2$).

51 of change, we can limit the hypothesis space, and so circumvent the degeneracy in the parameter
 52 estimation (see Figure 1). Our approach proceeds in two steps: First, we use simulated data
 53 generated from a forward model to train models that calculate how each parameter affects the
 54 measurements. Once these models of change have been trained for all hypothetical patterns of
 55 change, we use them to infer the posterior probability of which parameter(s) can best explain the
 56 change between real datasets. We call this approach BENCH, which stands for Bayesian EstimatiON
 57 of CHange.

58 When confronted with a degenerate biophysical model, BENCH makes a different set of
 59 assumptions from the traditional approach of fixing some parameters and identifying any change
 60 in the remaining free parameters. When comparing patients and controls, the traditional approach
 61 assumes that the prior values for the fixed parameters hold across the region of interest in both
 62 groups. Hence, any change of signal across the region of interest between the two groups is assumed
 63 to be fully explained by the predetermined set of free parameters. In contrast, by not relying on
 64 model inversion, BENCH can work directly with the degenerate biophysical model without fixing
 65 any parameters. However, this comes at the price of limiting the patterns of change to some

66 predetermined set of possible patterns of change set by the user (e.g., parameter A could change, or
67 parameter B increases by the same amount as parameter C decreases). While the number of such
68 proposed microstructural changes can be large, each of them has to be sparse (i.e., they have a lower
69 degree of freedom than the number of free parameters that could be estimated in the traditional
70 approach). In this work, we will limit ourselves to changes of just one parameter at a time.

71 BENCH is a general framework that is applicable to any situation where we are interested in
72 comparing parameters of a generative (bio)physical model across different conditions. Here we
73 apply the framework to dMRI microstructure modelling. As an example use case, we studied
74 microstructural changes in White Matter Hyperintensities (WMH), which are extra bright regions
75 that are commonly seen in T2-weighted images at specific brain regions in elderly people. Despite
76 the abundance and clinical implications of WMHs (Prins and Scheltens 2015; Debette and Markus
77 2010), the underlying changes in the histopathology and microstructure remain unknown (Wardlaw
78 et al. 2013).

79 The structure of this paper is as follows. In the Theory section, we present the general inference
80 method and how we train the models of change. In the Methods section, we cover the diffusion-
81 specific materials including the computation of summary measurements that are used to represent
82 diffusion data and the microstructural model for diffusion MRI. In the Results section, we first
83 demonstrate the ability of our model in detecting the underlying parameter changes using simulated
84 data. We then apply the method to study microstructural changes in white matter hyperintensities
85 as an example application. In the Discussion section, the potential applications, limitations, and
86 possible future directions of this work are presented.

87 THEORY

88 Inference on change in parameters

89 Given a baseline measurement (y), an observed change in the measurement (Δy), and a gen-
90 erative biophysical model (\mathcal{M}), we aim to investigate what pattern of change ($\hat{\Delta}v$) in the model
91 parameters (v) can best explain this observed change in the measurements (Figure 1). A pattern
92 of change is a unit vector in the parameter space, e.g. it can be a change in a single parameter, or

93 any linear combination of the model parameters. For simplicity of the explanations and notation,
94 we only assume a single parameter change in the rest of paper, but all the equations apply to any
95 linear combination of the parameters. If the model is invertible, we may directly estimate Δv by
96 inverting the model on y and $y + \Delta y$ to get the corresponding parameter estimates and calculate the
97 differences. Alternatively, in BENCH we estimate $P(\hat{\Delta v} | y, \Delta y)$, the posterior probability for the
98 pattern of change $\hat{\Delta v}$ conditioned on the observations y and Δy . Using Bayes' rule:

$$99 \quad P(\hat{\Delta v} | y, \Delta y) = \frac{P(\Delta y | y, \hat{\Delta v})P(\hat{\Delta v} | y)}{\sum_{\hat{\Delta v}'} P(\Delta y | y, \hat{\Delta v}')P(\hat{\Delta v}' | y)} \quad (1)$$

100 We assume no prior preference between the patterns of change (i.e. $P(\hat{\Delta v} | y)$ is uniform),
101 so to estimate the posterior probability distribution we only need to estimate the likelihood term
102 $P(\Delta y | y, \hat{\Delta v})$. The pattern of change $\hat{\Delta v}$ represents the direction but not the amount of the change
103 in the parameters. We therefore marginalize the likelihood with respect to the amount of change (
104 $|\Delta v|$):

$$105 \quad P(\Delta y | y, \hat{\Delta v}) = \int P(|\Delta v|)P(\Delta y | y, \hat{\Delta v}, |\Delta v|)d|\Delta v| \quad (2)$$

106 We assume that the prior distribution for the amount of change follows a log-normal pdf with a
107 fixed mean and scale parameter (adjustable hyper parameters). A log-normal PDF is chosen to
108 allow for changes across several order of magnitudes.

109 The likelihood term inside the integral, $P(\Delta y | y, \hat{\Delta v}, |\Delta v|)$, defines how the measurements change
110 as a result of a fully characterised vector of change in the parameters with the given direction ($\hat{\Delta v}$)
111 and amount ($|\Delta v|$). To relate this parameter change to a change in data one also needs to know the
112 baseline parameters (v), as

$$113 \quad \Delta y = \mathcal{M}(v + |\Delta v| \hat{\Delta v}) - \mathcal{M}(v) + \epsilon \quad (3)$$

114 where ϵ is the measurement noise. However, for a degenerate biophysical model, we cannot
115 estimate a unique set of baseline parameters v for which to estimate equation 3. While, one could
116 integrate over all possible values of v , this is a very high-dimensional integral, which would be very

117 computationally expensive. Instead, we propose an alternative way to avoid the need of estimating
118 the baseline parameters to estimate the likelihood.

119 Assuming that $|\Delta v|$ is reasonably small, and \mathcal{M} is behaving smoothly w.r.t v , using a Taylor
120 expansion we can express Δy as :

$$121 \quad \Delta y = \nabla_{\hat{\Delta}v} \mathcal{M}(v) |\Delta v| + \epsilon \quad (4)$$

122 Where $\nabla_{\hat{\Delta}v} \mathcal{M}(v)$ is the gradient of \mathcal{M} in the direction of $\hat{\Delta}v$ at point v , and ϵ is the measurement
123 noise. Given the baseline measurements (y), but not the baseline parameters (v), there can be an
124 infinite number of $\nabla_{\hat{\Delta}v} \mathcal{M}(v)$ for a degenerate model (Figure 2). To account for all instances of the
125 gradient, we model $\nabla_{\hat{\Delta}v} \mathcal{M}$ given y as a random variable that follows a normal distribution with
126 hyperparameters $\mu(y)$ and $\Sigma(y)$, i.e.

$$127 \quad P(\nabla_{\hat{\Delta}v} \mathcal{M} | y) = N(\nabla_{\hat{\Delta}v} \mathcal{M}; \mu_{\hat{\Delta}v}(y), \Sigma_{\hat{\Delta}v}(y)) \quad (5)$$

128 where $\mu_{\hat{\Delta}v}$ represents the average expected change in the measurements as a result of change in
129 parameters in the direction $\hat{\Delta}v$, $\Sigma_{\hat{\Delta}v}$ represents the uncertainty around this expectation due to the
130 unknown baseline parameters (Figure 2), and $N(x; m, C)$ represents a Gaussian PDF with mean m
131 and covariance C evaluated at point x . This allows us to transfer the uncertainty in the baseline
132 parameters to an uncertainty in the measurement space, which we can model and predict. In the next
133 section we will describe a method for estimating these hyperparameters from the measurements
134 by training regression models on simulated data. Once we compute these hyperparameters, by
135 inserting equation 5 back into equation 4 we can compute the likelihood term inside the integral as

$$136 \quad P(\Delta y | y, \hat{\Delta}v, |\Delta v|) = N(|\Delta v| \mu_{\hat{\Delta}v}, |\Delta v|^2 \Sigma_{\hat{\Delta}v} + \Sigma_n) \quad (6)$$

137 where Σ_n is the noise covariance matrix.

138 Finally, by computing the integral over the size of the parameter change in equation 2 numeri-

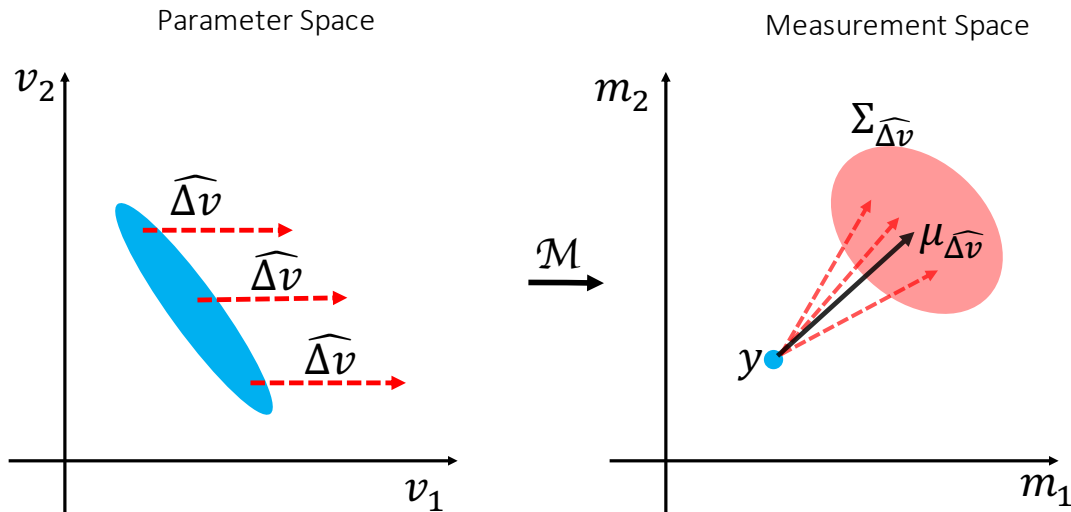


Figure 2. Distribution of gradients. The way measurements change as a result of a particular change in the parameters can only be calculated if we know the baseline parameters. When we are only given the measurements, there are several instances of equally likely gradient directions depending on the underlying baseline parameters. We model all of these gradients given the baseline measurements as a random variable with a presumed distribution. This allows us to transfer the uncertainty due to the inverse model degeneracy into the measurement space. The blue oval in the parameter space (left) represents all the parameter settings that map onto the same blue point in measurement space (right). Each of these parameter settings can produce a different gradient direction in the measurements space. The collection of such gradients of change $\hat{\Delta v}$ for the measurement y are modelled as a Gaussian distribution with mean $\mu_{\hat{\Delta v}}(y)$ and covariance $\Sigma_{\hat{\Delta v}}(y)$.

139 cally, we are able to approximate the likelihood function $P(\Delta y | y, \hat{\Delta v})$ which we can then use in
 140 equation (1) yielding the desired posterior distribution on the change in parameters.

141 Moreover, using the approximation of the likelihood function in equation 6 the posterior prob-
 142 ability of the amount of change in each parameter is proportional to

$$143 \quad P(|\Delta v| | \Delta y, y, \hat{\Delta v}) \propto P(\Delta y | y, \hat{\Delta v}, |\Delta v|) P(|\Delta v|) \quad (7)$$

144 Accordingly, we can estimate the most likely amount of change in the parameter given the measure-
 145 ments by finding the $|\Delta v|$ that maximizes the above posterior probability (maximum a posteriori
 146 estimation). Alternatively, we can estimate the expected value of the amount of change by integrat-
 147 ing this posterior probability distribution multiplied by $|\Delta v|$ over $|\Delta v|$.

148 Training models of change

149 In this section we describe how to train a regression model to estimate the hyperparameters of
150 the distribution of $\nabla_{\hat{\Delta}v} \mathcal{M}(v)$, namely the average ($\mu_{\hat{\Delta}v}(y)$) and uncertainty ($\Sigma_{\hat{\Delta}v}(y)$) of change in
151 the measurement (y) for a parameter change ($\hat{\Delta}v$).

152 Given some baseline parameters (v) we can calculate the baseline measurements as $y = \mathcal{M}(v)$
153 and approximate the gradient in direction $\hat{\Delta}v$ using

$$154 \nabla_{\hat{\Delta}v} \mathcal{M}(v) \approx \lim_{t \rightarrow 0} \frac{\mathcal{M}(v + t\hat{\Delta}v) - \mathcal{M}(v)}{t} \quad (8)$$

155 Therefore, by sampling v from the parameter space using a prior distribution, we generate a
156 simulated dataset of pairs $[y, \nabla_{\hat{\Delta}v} \mathcal{M}]$ that we use for training regression models.

157 We use a regression model parameterised by $w_{\mu_{\hat{\Delta}v}}$ to estimate $\mu_{\hat{\Delta}v}$ as:

$$158 \mu_{\hat{\Delta}v}(y; w_{\mu_{\hat{\Delta}v}}) = F(y) \cdot w_{\mu_{\hat{\Delta}v}} \quad (9)$$

159 where $F(y)$ is the design matrix, which depends on arbitrary affine or non-linear transformations of
160 y . Note that the subscript $\mu_{\hat{\Delta}v}$ of the weights indicates that each pattern of change in the parameters
161 has its own set of weights.

162 We also employ a regression model for the uncertainty hyperparameter $\Sigma_{\hat{\Delta}v}$ parameterised by
163 $w_{\Sigma_{\hat{\Delta}v}}$. However, $\Sigma_{\hat{\Delta}v}$ must be positive definite, which would not be guaranteed when directly
164 estimating $\Sigma_{\hat{\Delta}v}$ by training an element-wise regression model. To account for the positive definite
165 nature of $\Sigma_{\hat{\Delta}v}$, we instead train regression models for elements of the lower triangular matrix of
166 its Cholesky decomposition (L). Also, since the diagonal elements of the lower-triangular matrix
167 in Cholesky decomposition must be non-negative, we use their log-transform in the regression.
168 Hence

$$169 \Sigma_{\hat{\Delta}v}(y; w_{\Sigma_{\hat{\Delta}v}}) = \mathcal{T}(F(y) \cdot w_{\Sigma_{\hat{\Delta}v}}) \quad (10)$$

170 where \mathcal{T} is the transformation of the regressed vector to the full covariance matrix that includes

171 the arrangement of elements, exponentiation of the diagonals, and matrix multiplication.

172 Putting back the above regression models into equation 5 the likelihood of observing pairs of
173 baseline measurements and gradients in terms of the parameters of regression models is:

$$174 \quad L(w_{\mu_{\hat{\Delta}_v}}, w_{\Sigma_{\hat{\Delta}_v}}) = \prod_i N(\nabla_{\hat{\Delta}_v} \mathcal{M}_i; F(y_i) \cdot w_{\mu_{\hat{\Delta}_v}}, \mathcal{T}(F(y_i) \cdot w_{\Sigma_{\hat{\Delta}_v}})) \quad (11)$$

175 Accordingly, we estimate the optimal weights $w_{\mu_{\hat{\Delta}_v}}, w_{\Sigma_{\hat{\Delta}_v}}$ by maximizing the above likelihood
176 function for the simulated dataset using using a combination of the BFGS and Nelder-Mead methods
177 as implemented in SciPy ([Virtanen et al. 2020](#)).

178 This procedure is repeated for each hypothetical pattern of change, yielding two sets of weights
179 for the average and uncertainty of change, which we refer to as a “change model”. Once we
180 estimated these weights, for any given baseline measurement we use the regression models in
181 equations 9 and 10 to estimate the distribution of gradients. Figure 3 shows a schematic overview
182 of the inputs, outputs and steps that are required to train a change model, as well as how to use them
183 to infer the change in parameters.

184 In this work, we used a second degree polynomial function of the data for the regression models
185 that estimate the mean change ($\mu_{\hat{\Delta}_v}$) from the baseline measurements. For the uncertainty parameter
186 ($\Sigma_{\hat{\Delta}_v}$) a first degree (linear) model is chosen as we expect less variability across samples for this
187 parameter. The weights for the regression models were estimated using a maximum likelihood
188 optimization and a training dataset with 100,000 simulated samples.

189 **Biophysical model of diffusion**

190 In this section we explain the biophysical model of diffusion that we used to model brain
191 microstructure with diffusion MRI data. The diffusion signal S in the brain is conventionally
192 modelled as the sum of signals from multiple compartments. We will here adopt the three-
193 compartment standard model ([Novikov et al. 2019a](#)) consisting of an isotropic free water (denoted

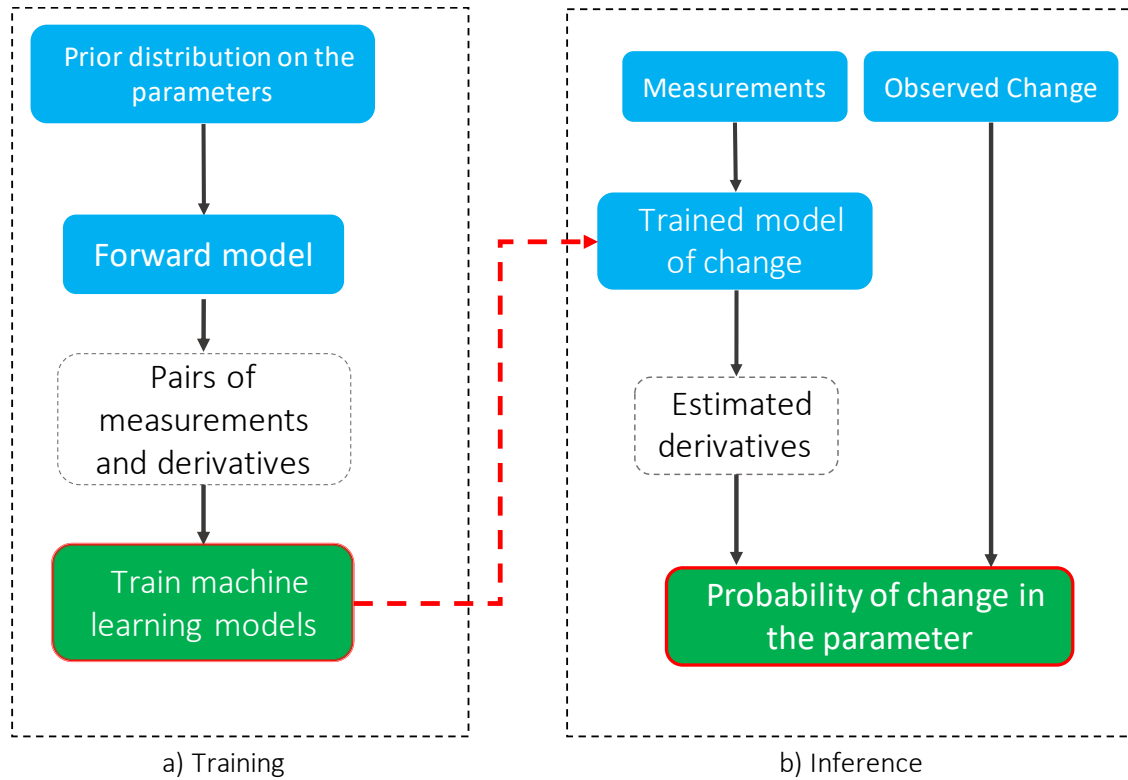


Figure 3. Schematic flowchart for training inference of change models. The blue, white and green blocks indicate user defined inputs, intermediate variables and outputs respectively. In the training phase for each parameter change, samples that are drawn from the provided prior distribution are passed through the forward model to estimate pairs of measurements and derivatives. Then, regression models are trained to estimate the distribution of derivatives given the measurements using a maximum likelihood estimation. This phase does not require real data and needs to be done only once. In the inference stage using these trained models we estimate the distribution of the derivatives for any given baseline measurements. We then calculate the posterior probability that change in each parameter caused the change in the measurements using the derivative distributions.

194 by the subscript “iso”), an intra-axonal (“in”), and an extra-axonal (“ex”) compartment:

$$195 \quad S = S_{iso}A_{iso} + S_{in}A_{in} + S_{ex}A_{ex} \quad (12)$$

196 where S_i represents the baseline signal contribution (at $b = 0$), and A_i represents the signal
197 attenuation due to the diffusion weighting in each compartment (Figure 4).

198 The attenuation for the isotropic compartment is modelled as an exponential decay:

$$199 \quad A_{iso} = e^{-bd_{iso}} \quad (13)$$

200 where d_{iso} is the diffusion coefficient of free water.

201 The intra-axonal compartment is modelled as a set of dispersed identical sticks with no per-
 202 pendicular diffusivity. Therefore, the signal attenuation for this compartment is the spherical
 203 convolution of a stick response function with an orientation distribution function. The stick re-
 204 sponse function for gradient direction g and b-value b is given by

$$205 \quad R(b, g; \mu, d_{in,a}) = e^{-bd_{in,a}(\mu^T g)^2} \quad (14)$$

206 where $d_{in,a}$ is the diffusion coefficient along the orientation of the stick μ . The fibre Orientation
 207 Distribution Function (fODF) is modelled with a Watson distribution, which is defined as

$$208 \quad f(x) = \frac{1}{c} e^{\kappa(\mu^T x)^2} \quad (15)$$

209 where μ is the average orientation, κ is the concentration coefficient and c is a normalization
 210 constant. To assimilate the dispersion coefficient to the notion of variance and limit it to a
 211 bounded range, we use the change of variable from κ to Orientation Dispersion Index (ODI) as
 212 $ODI = \frac{2}{\pi} \arctan(\frac{1}{\kappa})$. Unlike κ which is unbounded, ODI is limited to the range $(0, 1)$, where
 213 higher ODI values correspond to more dispersion. The diffusion signal for this compartment is
 214 the spherical convolution of the fiber response function with the Watson ODF:

$$215 \quad A_{in} = \iint_{S^2} e^{-bd_{in,a}(g^T n)^2} \frac{1}{c} e^{\frac{2}{\pi} \tan^{-1}(ODI)(\mu^T n)^2} dn \quad (16)$$

216 where the integral is over the surface of the unit sphere S^2 representing all possible fibre orientations
 217 in 3D.

218 The extra-axonal compartment is modelled similar to the intra-axonal compartment, with the
 219 addition of a non-zero diffusion perpendicular to the fiber orientation. The fiber response function
 220 in this case is given by

$$221 \quad R = e^{-b[d_{ex,a}(\mu^T g)^2 + d_{ex,r}(1 - (\mu^T g)^2)]} \quad (17)$$

222 where $d_{ex,r} \leq d_{ex,a}$ is the radial diffusion coefficient. To avoid this dependence between the
 223 diffusivity parameters, the parameter τ defined as the ratio of perpendicular to parallel diffusivity is
 224 used as a substitute to $d_{ex,r}$. The free parameter τ - subject to $\tau \in [0, 1]$ to maintain the inequality
 225 constraint for the diffusivities - can be considered as a measure of tortuosity as it measures the
 226 extent to which water diffusion perpendicular to the fibre orientation is hindered with respect to the
 227 parallel diffusion. Therefore, the fiber response function for the extra axonal compartment is

$$228 \quad R = e^{-bd_{ex,a}[(\mu^T g)^2 + \tau(1 - (\mu^T g)^2)]} \quad (18)$$

229 As the compartments share the same geometry, the same fibre orientation distribution is used.
 230 Accordingly, the signal attenuation for extra-axonal compartment is given by

$$231 \quad A_{ex} = \iint_{S^2} e^{-bd_{ex,a}[(\mu^T g)^2 + \tau(1 - (\mu^T g)^2)]} \frac{1}{c} e^{\frac{2}{\pi} \tan^{-1}(ODI)(\mu^T n)^2} dn \quad (19)$$

232 We use the confluent hypergeometric function of the first kind with matrix argument to compute
 233 the integrals for both intra and extra axonal compartments similar to (Sotiropoulos et al. 2012).

234 Table 1 reports all the free parameters of the described biophysical diffusion model along with
 their valid range.

| Parameter | Description | Range |
|------------|--|----------------|
| s_{iso} | Signal fraction for isotropic (free water) diffusion compartment | [0, 1] |
| s_{in} | Signal fraction for intra-axonal compartment | [0, 1] |
| s_{ex} | Signal fraction for extra-axonal compartment | [0, 1] |
| d_{iso} | Isotropic (free water) diffusivity coefficient | [0, ∞] |
| $d_{in,a}$ | Parallel diffusivity for the intra-axonal compartment | [0, ∞] |
| $d_{ex,a}$ | Parallel diffusivity for the extra-axonal compartment | [0, ∞] |
| τ | radial to axial diffusivity ratio for the extra-axonal compartment | [0, 1] |
| ODI | Orientation dispersion index | [0, 1] |

TABLE 1. Microstructural parameters of the diffusion model. All diffusion coefficients are in $\mu m^2/ms$

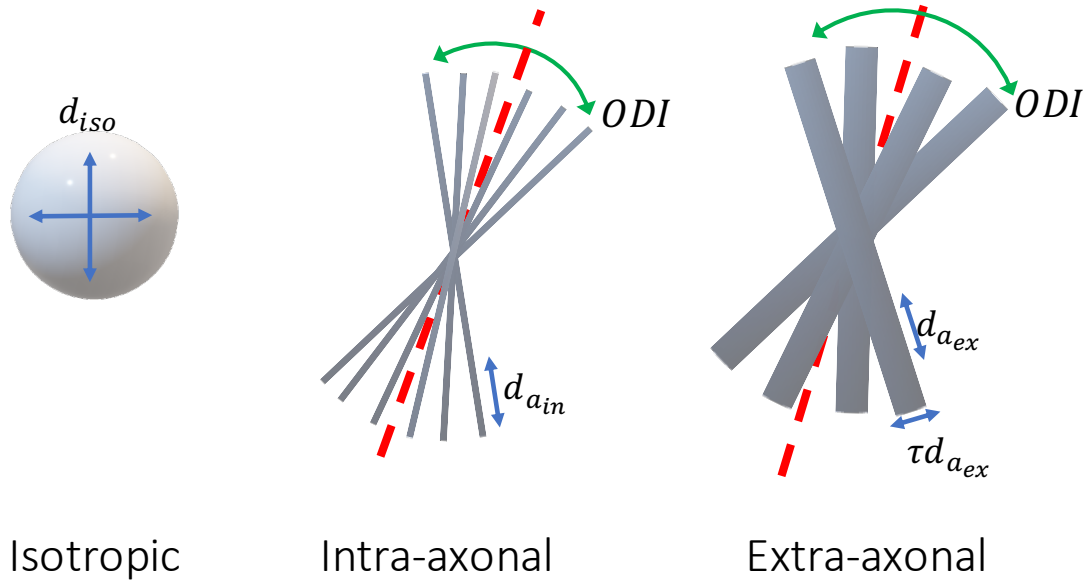


Figure 4. Compartments of the diffusion model. We use a three compartment model that can model diffusion MRI signals from various brain tissues namely CSF, white matter and gray matter. The isotropic compartment models unrestricted diffusion of water molecules outside of tissue (CSF) with a single free parameter d_{iso} . The intra-axonal compartment models the diffusion of water within axons as several sticks with the same parallel diffusivity parameter $d_{in,a}$, with zero radial diffusivity, that are dispersed by a Watson distribution with orientation dispersion index ODI . The extra-axonal compartment is also a Watson dispersed stick model with parallel diffusivity $d_{ex,a}$ and perpendicular diffusivity $d_{ex,r} = \tau d_{ex,a}$. Including the signal fraction parameters (s_{iso}, s_{in}, s_{ex}) this model has 8 free parameters, which are more than that can be fitted to a conventional dMRI data.

Summary measurements

Diffusion MRI data are usually measured in multiple shells to capture tissue properties that are sensitive to diffusion of water molecules at various spatial scales. Within each shell, gradients are applied in several directions to measure the geometrical structure of the tissue. However, since we are only interested in the microstructural characteristics, any orientation-related information is irrelevant. We therefore need summary measurements from each shell that are invariant to orientations. We create these summary measurements using real spherical harmonics, which are analogous to the Fourier transform for the spherical domain.

Spherical harmonics are a complete set of orthonormal functions over the surface of a unit sphere. That is to say, any bounded real function that is defined over the unit sphere can be represented by a unique linear combination of these functions with real coefficients. Each real spherical harmonic is denoted by $Y_{l,m}(\theta, \phi)$ where $l = 0, 1, 2, \dots$ is the degree and $m = -l, \dots, l$ is

248 the order, and $\theta \in [0, \pi]$, $\phi \in [-\pi, \pi]$ are the polar and longitudinal angles in standard spherical
249 coordinate system respectively. The diffusion signal at each shell is decomposed as:

$$250 \quad S(\theta, \phi) = \sum_{l=0}^{\infty} \sum_{m=-l}^l C_{l,m} Y_{l,m}(\theta, \phi) \quad (20)$$

251 Since the harmonics are a linear basis, one can easily calculate the coefficients for the signal in each
252 shell by inverting the design matrix formed by the harmonics sampled at the gradient directions.

253 The coefficients are not orientationally invariant. However, the total power in each degree,
254 which is defined as the vector norm of all the coefficients in that degree, is rotationally invariant
255 (Kazhdan et al. 2003; Zucchelli et al. 2020; Novikova et al. 2018). Also, since the diffusion signal
256 is symmetric around the origin and the harmonics of odd degree are odd functions (anti-symmetric
257 w.r.t origin), all odd degrees have zero coefficients.

258 Consequently, for each shell of diffusion data, we calculate the mean squares of all coefficients
259 for degrees $l = 0, 2, 4, \dots$ as the orientationally-invariant summary measurements.

$$260 \quad y_l = \frac{1}{2l+1} \sum_{m=-l}^l C_{l,m}^2 \quad (21)$$

261 The mean is chosen over the norm to make the scale equal across all degrees. For the case of
262 $l = 0$, we simply use the only coefficient (without the square), so that it represents the mean signal.
263 The higher order summary measurements quantify the signal anisotropy; with greater l being more
264 sensitive to sharper changes. We used a logarithm transformation on the power of the coefficients
265 to make the distribution across the brain closer to a Gaussian and more sensitive to smaller changes.

266 METHODS

267 Simulations

268 For all the simulations we used the acquisition protocol conducted by the UK Biobank (UKB)
269 (Miller et al. 2016; Alfaro-Almagro et al. 2018) which includes two shells of diffusion ($b = 1, 2 \frac{\text{ms}}{\mu\text{m}^2}$)
270 with linear diffusion encoding. Each shell consists of 50 gradient directions distributed uniformly

271 over the surface of the unit sphere, in addition to 5 acquisitions with $b = 0$, yielding a total of 105
272 measurements.

273 We used the rotationally invariant summary measurements computed from spherical harmonics
274 for signal representation. The summary measurements for each shell are norms of coefficients at
275 $l = 0$ (absolute value) and $l = 2$ (log mean squared). This produces 5 rotational invariant summary
276 measurements from a diffusion data, namely $b0\text{-mean}$, $b1\text{-mean}$, $b1\text{-l2}$, $b2\text{-mean}$, and $b2\text{-l2}$.

277 The described standard model for diffusion is used for both simulated test data and for training
278 models of change. The prior distributions for the parameters are shown in figure 5. We note that
279 these priors are not used for constraining the model parameters but rather they are used to generate
280 training samples for the regression models. The choice of the prior distributions is arbitrary as long
281 as they can reflect all hypothetical parameter combinations that can produce measurements similar
282 to real data.

The standard model is not invertible given a conventional multishell diffusion data with linear
diffusion encoding (Novikov et al. 2019a; Jelescu et al. 2016). Typically, additional constraints
are imposed to render the model invertible, e.g. in NODDI (Zhang et al. 2012), the diffusion
coefficients are fixed to a prior value as follows:

$$d_{iso} = 3 \frac{\mu m^2}{ms}, d_{in,a} = d_{ex,a} = 1.7 \frac{\mu m^2}{ms}$$

283 Additionally, the tortuosity parameter τ is coupled to the signal fractions:

$$284 \tau = \frac{s_{in}}{s_{in} + s_{ex}} \quad (22)$$

285 Accordingly, this constrained model has four free parameters: s_{iso} , s_{in} , s_{ex} and ODI .

286 For both the constrained and unconstrained models, we generated a test dataset containing
287 pairs of simulated diffusion signals, such that in each pair at most one microstructural parameter is
288 different. To generate each pair, we sample a baseline parameter setting from the prior distributions
289 and change one of the parameters by an effect size of 0.1. We also generate pairs of data where no

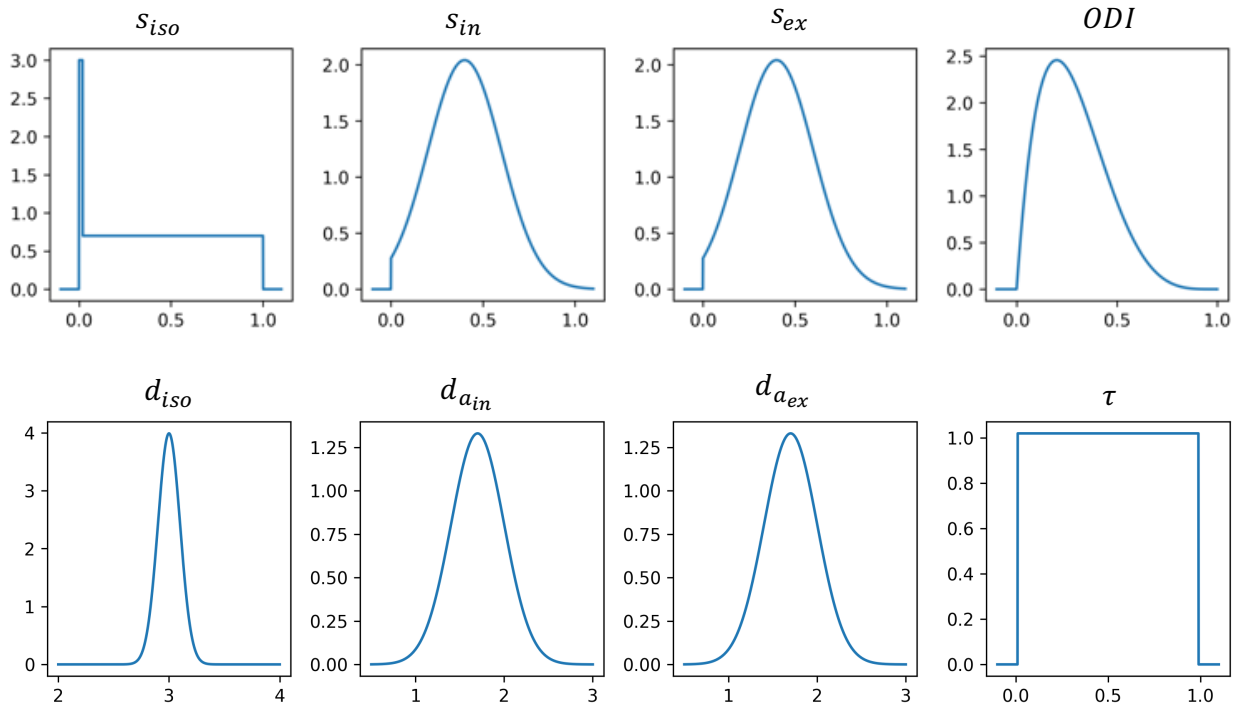


Figure 5. Prior distributions for the parameters of the standard model. These priors are used for generating pairs of measurements and gradients for training the models of change. Also, the same priors are used for simulating test datasets. The priors are chosen such that they contain all probable parameter combinations that can produce measurements similar to real data. The delta function along with uniform distribution in the isotropic signal fraction is used to model pure tissue types as well as partial volume effect. In the training phase, the volume fractions are normalized to sum up to 1. A beta (shape parameters $\alpha = 2, \beta = 5$) distribution is used for ODI to impose a uniform distribution for effective fibre dispersion. The prior for isotropic and axial diffusivities are normal distributions with mean 3 and 1.7 ($\frac{\mu m^2}{ms}$) and standard deviation 0.1 and 0.3 respectively; as we expect faster diffusion as well as less variability in the free water component.

290 parameter changes and the difference between the two samples is only due to the addition of noise.
 291 We then apply the forward model to both parameter settings to produce diffusion MRI signals.
 292 Gaussian noise with standard deviation $\sigma_n = 0.02$ (SNR=50) is added to all diffusion signals.

293 The signal fraction parameters are constrained to sum up to 1 for training models of change.
 294 Note that whilst this imposes a constraint that the *b0-mean* for the baseline measurement is equal
 295 to 1, it does not constrain a *change* in that summary measurement. Accordingly, all the summary
 296 measurements (both in the baseline and the change vector) are normalized by the *b0-mean* of the
 297 baseline measurement for any real data. This differs from the conventional NODDI, where there is a
 298 constraint on the signal fractions to sum up to 1 for each sample, which reduces the free parameters

299 to 3, but here we assume all the parameters can change independently.

300 For the direct inversion approach, a maximum a-posteriori algorithm is employed to estimate
301 the parameters of the constrained model from each diffusion signal separately. Then using a z-test
302 across the parameter estimates in each pair, we calculate a p-value for the change in each parameter
303 (corrected for multiple comparisons across parameters). The parameter with the minimum p-value
304 is identified as the changed parameter. All the cases with minimum $p > 0.05$ are identified as no
305 change.

306 We also used BENCH for identifying change on the same dataset. To estimate the noise
307 covariance in the summary measurements Σ_n , 100 noisy instances of signals were generated, and
308 the sample covariance of the difference between summary measurements in each pair was estimated.
309 We then estimated the posterior probability of change in each parameter using the trained models
310 of change. The *no change* model has a zero mean and covariance Σ_n everywhere. The change
311 model with the maximum posterior probability is selected as the predicted change.

312 **White matter hyperintensities**

313 We employed the trained models of for the parameters of the standard model to investigate
314 the microstructural changes in white matter hyperintensities (WMH). In this experiment, we used
315 diffusion MRI of 2400 randomly selected subjects from the UK biobank dataset. To account for
316 the variability in overall intensity across subjects, we divided each subject's diffusion data by the
317 average intensity of the b0 image across the brain's white and grey matter extracted using FSL FAST
318 (Zhang et al. 2000). We then computed the spherical harmonics-based summary measurements
319 from the diffusion MRI data for each subject and interpolated these measures into the standard MNI
320 space using non-linear transformations estimated by FSL FNIRT (Woolrich et al. 2009; Andersson
321 et al. 2019).

322 Segmentations of the WMHs were generated from T2 FLAIR images using FSL's BIANCA
323 (Griffanti et al. 2016) as part of the UK Biobank pipeline (Miller et al. 2016). We computed
324 the average summary measurements for normally appearing white matter (voxels within the white
325 matter mask not classified as WMH) and the WMHs for all voxels that included more than 10

326 subjects with WMH. For each voxel, subjects were split into two groups according to whether the
327 voxel has been classified as WMH or not. Averaging the summary measures within groups provides
328 us with the baseline measurement (y) and the observed change (Δy) related to WMH. The noise
329 covariance (Σ_n) in each voxel was estimated using the within group covariance matrix divided by
330 the number of subjects in the normal appearing white matter group.

331 RESULTS

332 Summary measures

333 A representative axial slice of the normalized summary measurements from a single subject are
334 shown in Figure 6. The "*mean*" summary measures represent the normalised average signal. The
335 $l2$ measures quantify the anisotropy in each voxel (similar to Fractional Anisotropy maps in DTI).

336 The bottom panels of Figure 6 show histograms of the summary measurements across the brain
337 for the same subject, as well as distributions of simulated data based on prior distributions over the
338 model parameters. The distribution for the generated samples fully covers the range of the data and
339 follows the same density distribution. This verifies that the prior distributions are wide enough to
340 capture the full range of real data.

341 Figure 7 shows estimated derivatives of the summary measurements at baseline data repre-
342 sentative of putative voxels in the white matter and grey matter. The error bars show estimated
343 standard deviations of the derivatives (the square root of diagonals of the estimated covariance
344 matrix). This variance is reflecting the uncertainty in the underlying parameters that can generate
345 these measurements, as well as residuals of the regression model for the mean.

346 Simulations

347 We first employed simulated data to evaluate the performance of the proposed approach in
348 inferring microstructural changes from diffusion MRI data.

349 *Comparison with model inversion*

350 Figure 8 shows the confusion matrix using model inversion (left), and our inversion-free
351 approach (right) for an invertible model with only 4 free parameters. Each element of these matrices

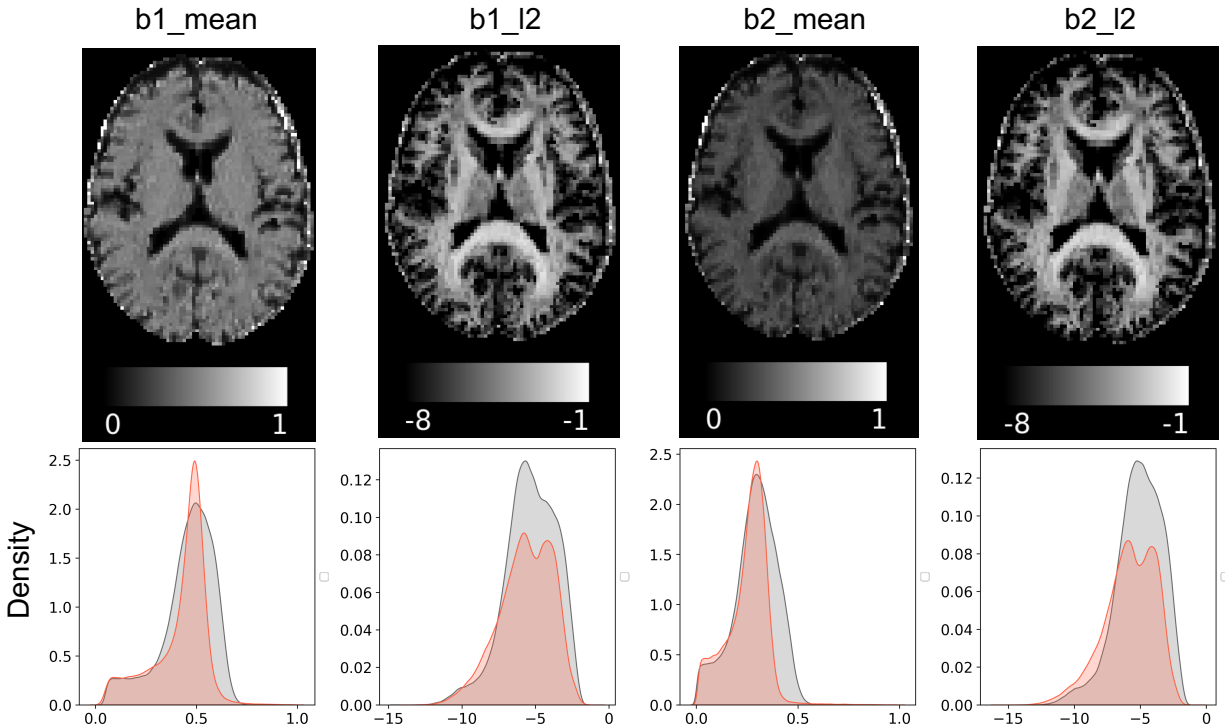


Figure 6. Maps of the summary measurements for a sample subject in the UK biobank dataset (top) and their histogram (bottom). The mean summary measurements is reflecting the mean diffusivity in each shell. The $l2$ summary measurements estimate the anisotropy, which is similar to the fractional anisotropy (FA), but computed with a linear transformation of the signal. Histograms show the distribution of these measurements across the brain; as well as the distribution of simulated data using the standard model and provided prior distributions. This shows that the simulations capture the full range of the summary measures from real data.

352 represents the percentage of times a change in the parameter represented at the corresponding
353 column is identified as a change in the corresponding row. Both approaches were able to detect the
354 true change in most of the cases.

355 For the standard model with all 8 free parameters, Figure 9 shows the confusion matrices
356 using the direct model inversion (left) and change estimation (right). Since the uncertainties of the
357 parameter estimates are very large due to the model degeneracies, almost all of the changes are
358 confused with *no change* when using direct inversion. However, the inversion-free approach is able
359 to identify changes in s_{iso} , s_{in} , s_{ex} and ODI . Although, there is confusion between the remaining
360 parameters compared to the restricted model, here we do not make any strong assumptions on
361 the value of those parameters. Also, most of the confusions for these parameters are between
362 them, meaning that we are able to distinguish a change in those parameters (e.g. the diffusivity

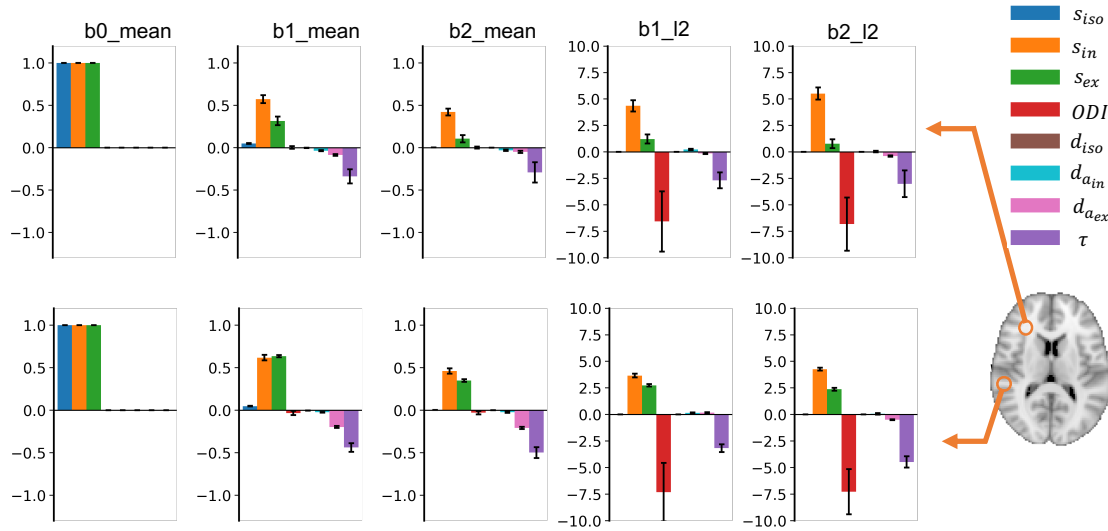


Figure 7. The estimated amount of change in the summary measurements as a result of a unit change in each parameter (μ_{Δ_v}) for a sample white matter and grey matter voxel. The error bars show the estimated standard deviation of change. Colors correspond to parameters and columns indicate summary measurements. Due to differences in the baseline, each voxel can have a different change vector for the same parameter change. This added degree of freedom can model the variability of parameters (e.g. diffusivities) across the brain, which is not considered in restricted models; e.g. NODDI.

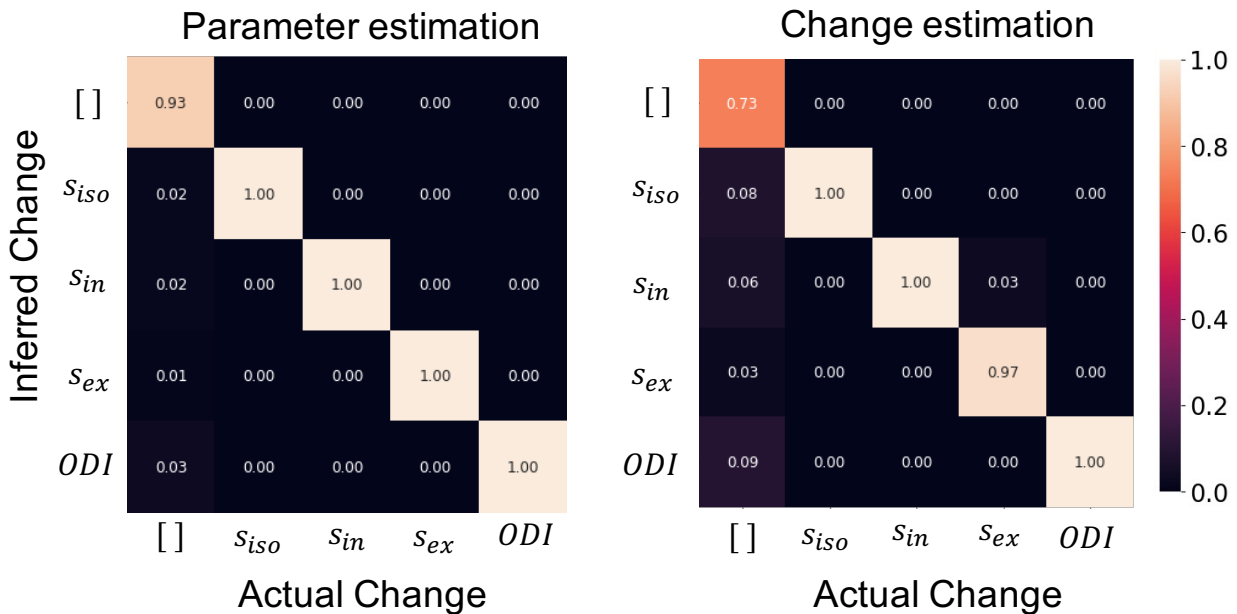


Figure 8. Confusion matrices for the constrained model using the direct inversion and the proposed approach. The numbers indicate the percentage of time a change in the corresponding column is identified as a change in the corresponding row for each approach. The diagonal elements show the accuracy in identifying true change. Both of the approaches performed near to ideal in detecting the true change. The change estimation has more false positives, but unlike the inversion approach, we did not explicitly define a false positive rate threshold.

363 parameters) from others. Change in isotropic diffusivity is mostly confused with the *no change*
 364 model. This is due to the *b*-values in the UKB protocol which are too high for this parameter;
 365 a change in this parameter has minimal effect on the signal. The changes in parallel diffusivity
 366 parameters $d_{in,a}$, $d_{ex,a}$ are mostly detected correctly or confused with one another. This is because,
 367 specifically at low tortuosity, these two parameters affect the diffusion signal in a similar way.

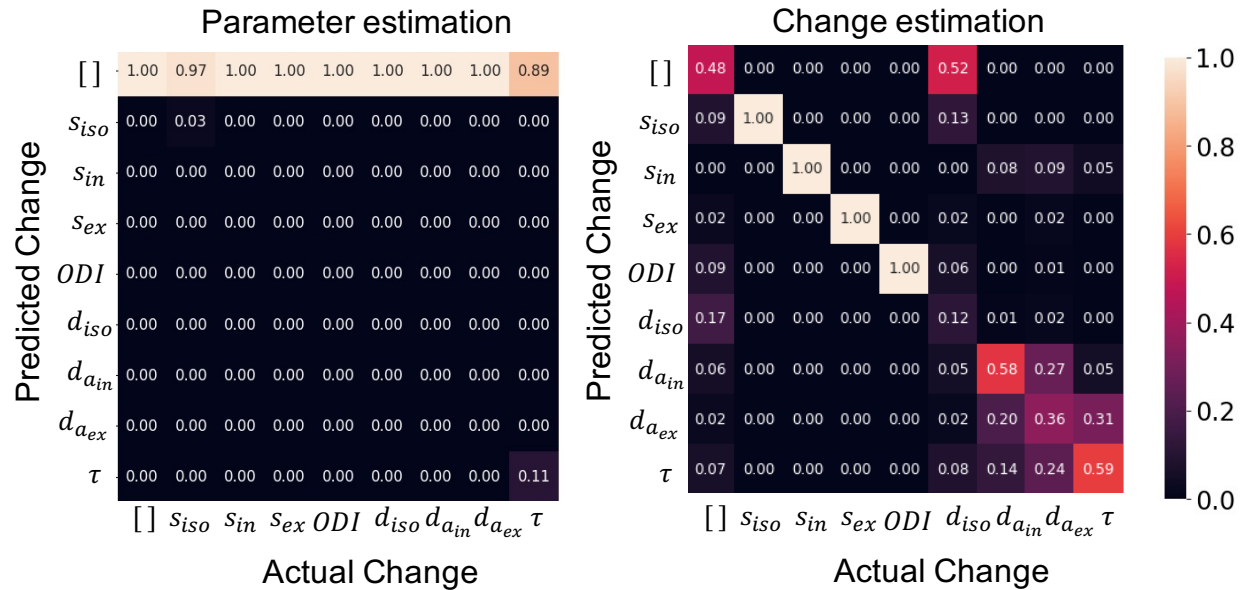


Figure 9. Confusion matrices for the full model using parameter estimation (left) and change estimation (right). Given diffusion data at few shells, the full model is not invertible, i.e. the parameter estimates have a high variance. Therefore, almost no significant change is detected using parameter estimates. On the other hand, the change estimation approach can still identify changes in all the parameters of the restricted model. Although there remains confusion between a subset of the parameters when these have similar effects on the diffusion signal

368 *Sensitivity to change in each parameters*

369 To evaluate the sensitivity of the approach to the amount of change in each parameter, we
 370 generated test datasets with variable effect sizes starting from 0 to 0.15 with step sizes of 0.01.
 371 Figure 10 shows the average posterior probability of change in each parameter versus the effect
 372 size. In all types of change, at very small effect sizes (< 0.01) the change is confused with no
 373 change, but as the effect size increases the probability of identifying the true change (red curves)
 374 increases. Changes in all signal fraction parameters and in the fibre dispersion are identified with
 375 high accuracy even at very small effect sizes (note that these are the parameters allowed to vary

376 freely in NODDI). However, changes in diffusivity parameters are confused with each other (but
 377 not with signal fraction parameters) even at larger effect sizes.

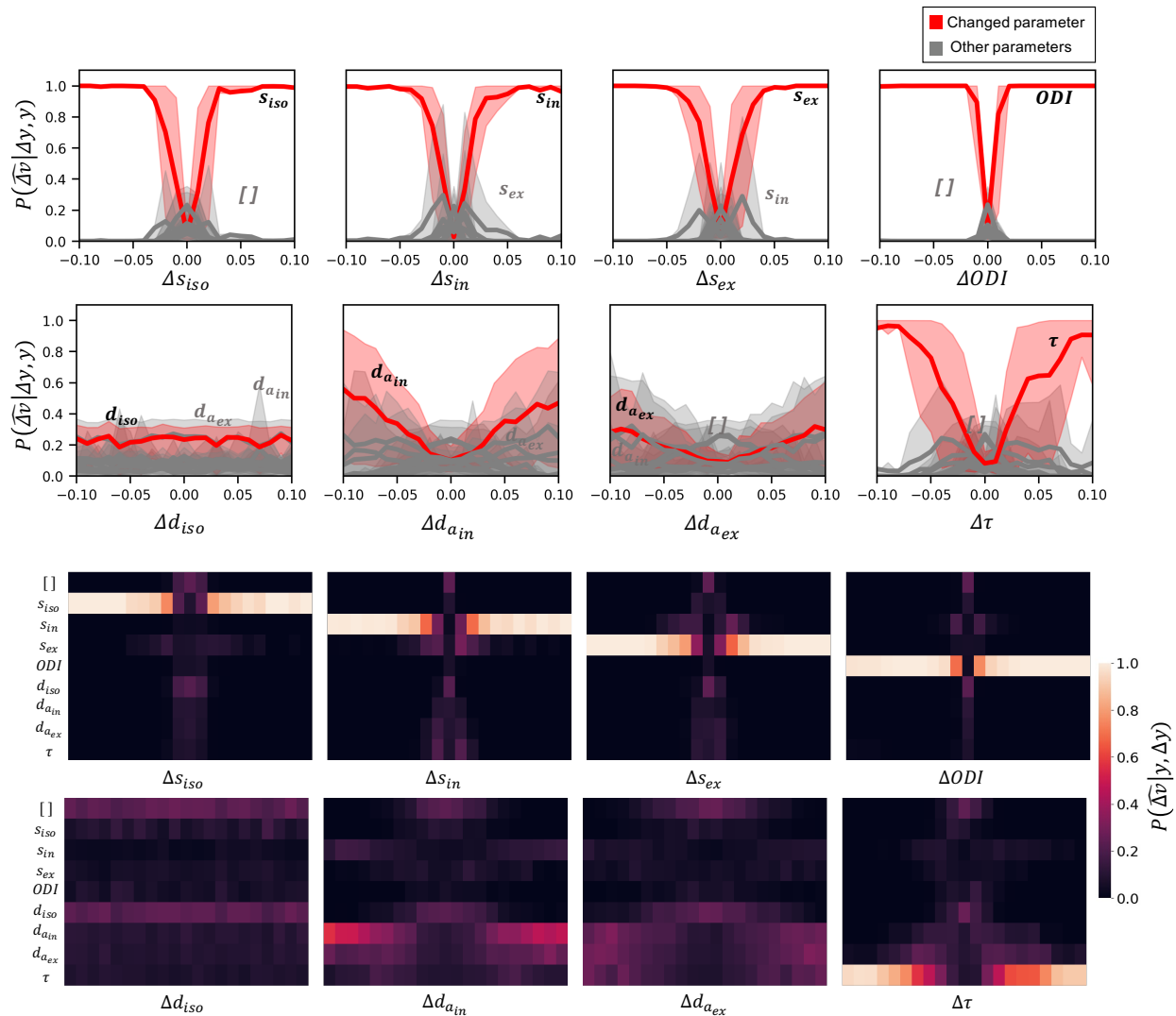


Figure 10. Sensitivity to the amount of change in the parameters of the standard model. Top: Red curves show the average posterior probability of change in the actual changed parameter as a function of the amount of change. The gray curves show the posterior probability for other parameters. Shaded areas show the 90 percentile range. Larger absolute amount of change results in higher posterior probability for the true parameter change. Change in the signal fraction parameters and *ODI* is distinguishable for effect sizes as small as 0.05. However, changes in diffusivity parameters even at very large effect sizes is cluttered with other parameters. Bottom: The same plots shown as heatmaps to better visualize which parameters are confused with each other.

378 *Estimating the amount of change*

379 So far we have only examined the posterior probabilities relating to the identity of the parameters
380 that can best explain a change. However our framework also allows us to estimate the posterior
381 probability on the *amount* of change for each parameter $P(|\Delta v| \mid y, dy, \hat{\Delta}v)$ (eq.7). Figure 11
382 shows the estimated (maximum a posteriori estimation) versus actual change in each parameter for
383 different effect sizes.

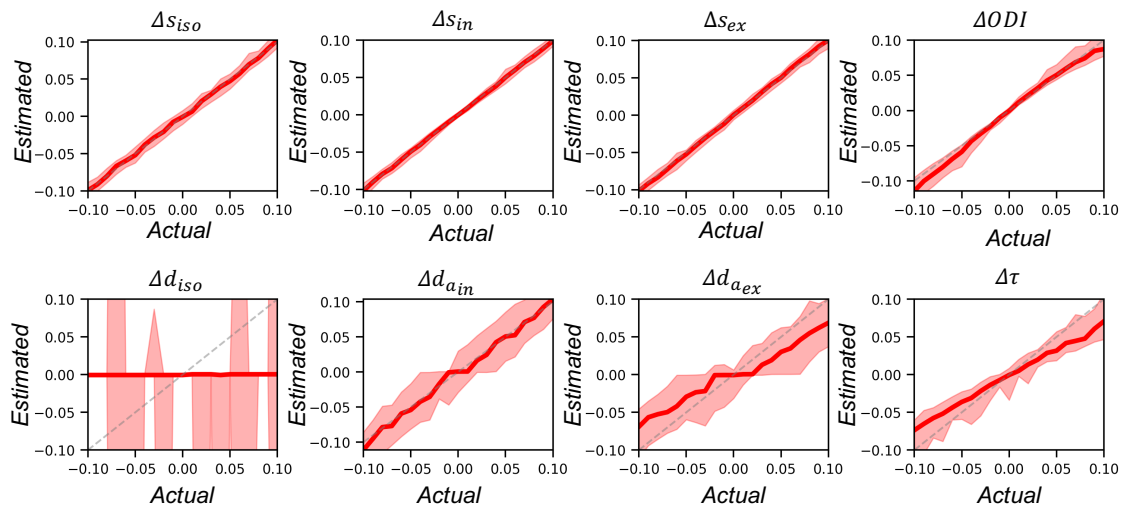


Figure 11. Estimated amount of change in each parameter. Each plot shows the median of the estimated (maximum a posteriori) change vs the actual change in the parameter. The shaded areas show the 10% interval. The estimated change in the signal fractions follow the identity line (dashed gray line). The estimated change in d_{iso} is mostly around zero with a high variance as the posterior distribution is very flat and symmetric around zero. The change in $d_{ex,a\tau}$ and ODI is systematically biased at higher effect sizes.

384 **White matter hyperintensities**

385 Figure 12 shows the observed and estimated amount of change in the summary measurements
386 due to change in each parameter for average data from a small patch in white matter. The last bar
387 in each panel shows the average and standard deviation (across voxels) of the observed amount of
388 change due to WMH normalized by the $mean_b0$ of the baseline measurement. For each parameter
389 the best amount of change given the baseline, observed change and noise covariance is estimated
390 using equation 3. The bars indicate the amount of change in the measurements that the estimated
391 change in the corresponding parameter can produce.

392 The observed change in WMH is an increase in the $b0_mean$ and $b1_mean$ as well as an increase
 393 in anisotropy for the $b1_shell$. This pattern of change is better aligned with a positive change in s_{ex}
 394 than in any other parameter.

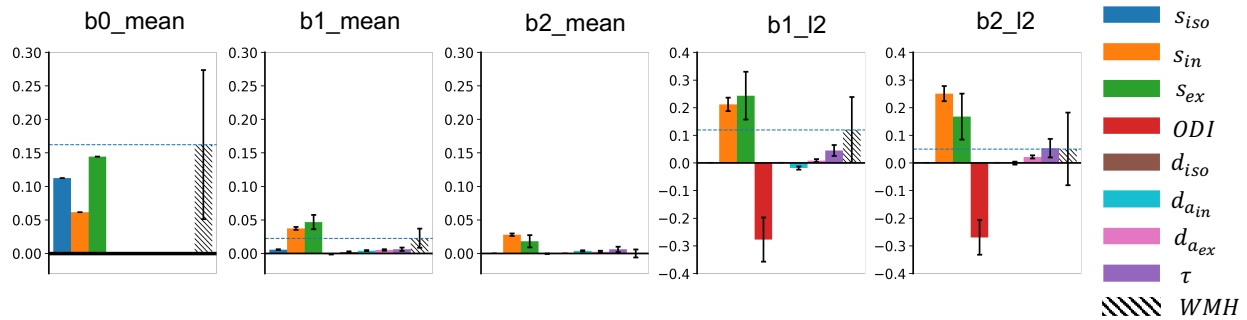


Figure 12. Estimated change vectors along with change in white matter hyperintensities. Each panel shows the estimated amount of change in the measurements if only the corresponding parameter changes, along with the actual observed change in hyperintensities for a patch of voxels in white matter. Each bar is scaled with the best estimated amount of change for that parameter. The observed change in WMH is an increase in the $mean-b0$ and, to a lesser extent, and increase in $mean-b1$, and a positive change in the $l2$ measurements. This is best aligned with the pattern of change that an increase in s_{ex} can produce.

395 Figure 13 shows the estimated probability of change $P(\hat{\Delta}v | \Delta y, y)$ for each parameter of the
 396 standard model for an axial slice of the brain in voxels that included more than 10 WMH subjects.
 397 These probabilities are normalized to sum up to 1 for each voxel. The colors indicate the probability
 398 that a change in the corresponding parameter can explain the observed changes due to WMHs.

399 Figure 14 shows the best explaining model of change in each voxel in a few axial slices of the
 400 brain. In more than 65% of the voxels, that are mostly in deep white matter, the best model is a
 401 change in s_{ex} . However, in voxels adjacent to the ventricles, all other models compete and there
 402 is not a dominantly winning model. This might be due to a true difference in microstructure in
 403 these periventricular voxels, or may be caused by high variability across subjects due to CSF partial
 404 volume effects.

405 Figure 15 shows the estimated amount of change in s_{ex} in voxels where this was the most
 406 probable parameter. In most of the voxels an increase in s_{ex} between 0 and 0.4 explains the
 407 observed change in WMH. The bottom right panel shows that the amount of change increases with
 408 distance from the ventricles, whereas in deep white matter the average amount of change remains

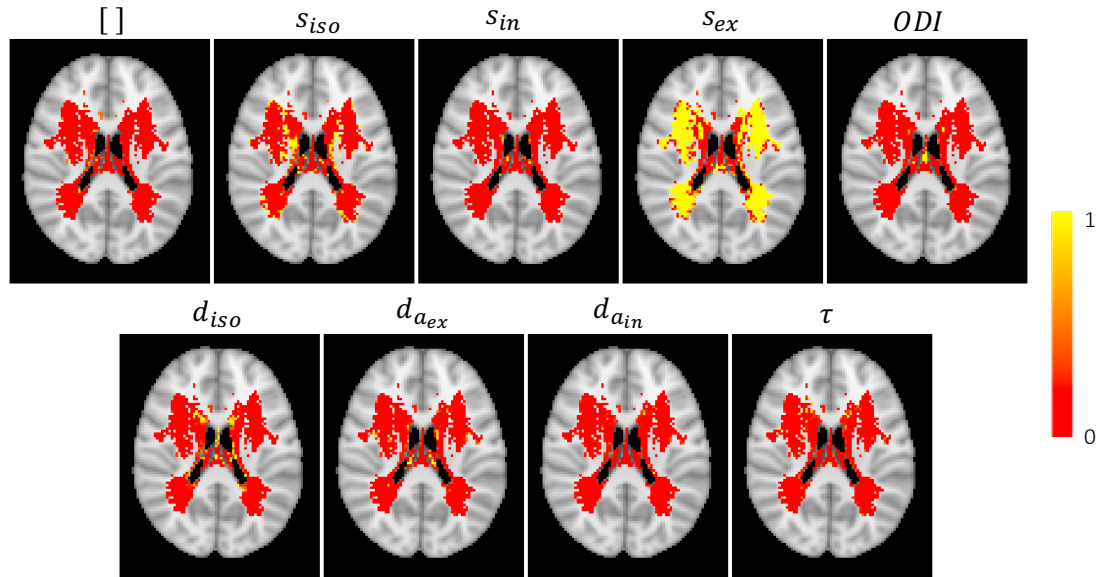


Figure 13. Posterior probability of change in each parameter $P(\hat{\Delta}_v | \Delta y, y)$. Each map shows the estimated probability that change in the corresponding parameter can explain the observed change in the summary measurements from diffusion MRI between white matter hyperintensities and normally appearing white matter at a single axial slice of the brain. The no change model represents the null model that the change is better explained by noise rather than a change in any one of these parameters. In the majority of the voxels, the change model for s_{ex} has a probability around 1 (yellow) and the remaining parameters are nearly zero (red). This means that a change in s_{ex} is more likely to explain the observed change than any other single parameter change.

409

relatively constant.

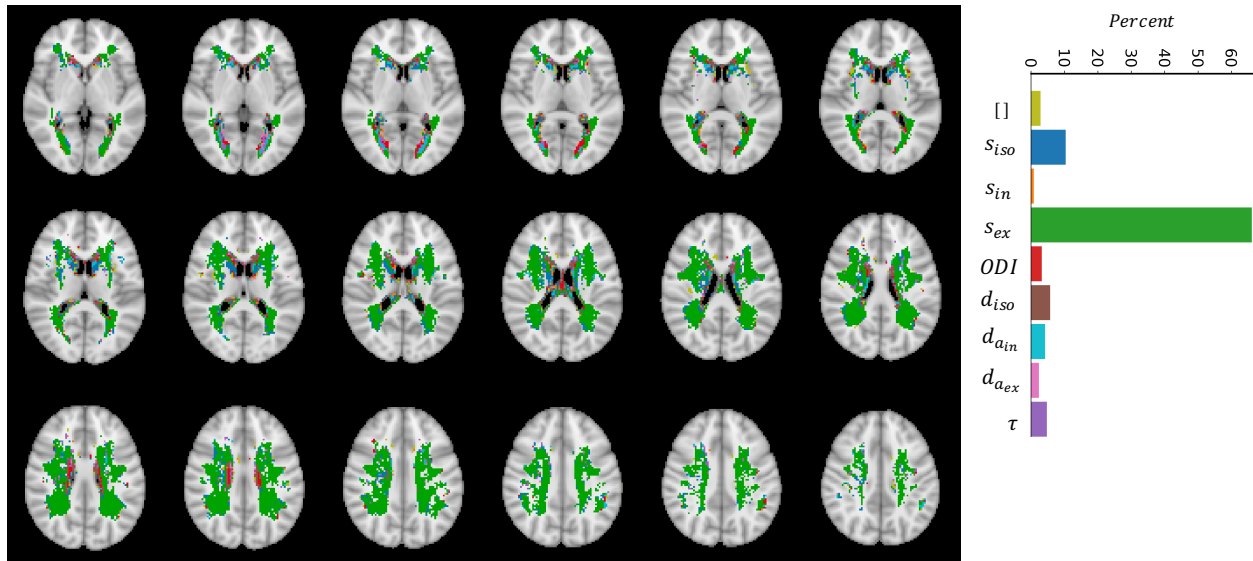


Figure 14. Best explaining model of change in each voxel. The colors indicate which model of change could best explain, i.e. had the highest posterior probability given the observed change in the summary measurements between WMH and normally appearing white matter. In the majority of voxels (68%) a change in s_{ex} explained the data better than any other model. However, in the regions very close to the ventricles there is no major winning model. This can be either because of high between subject variability or a different type of change that is not captured by the trained models of change.

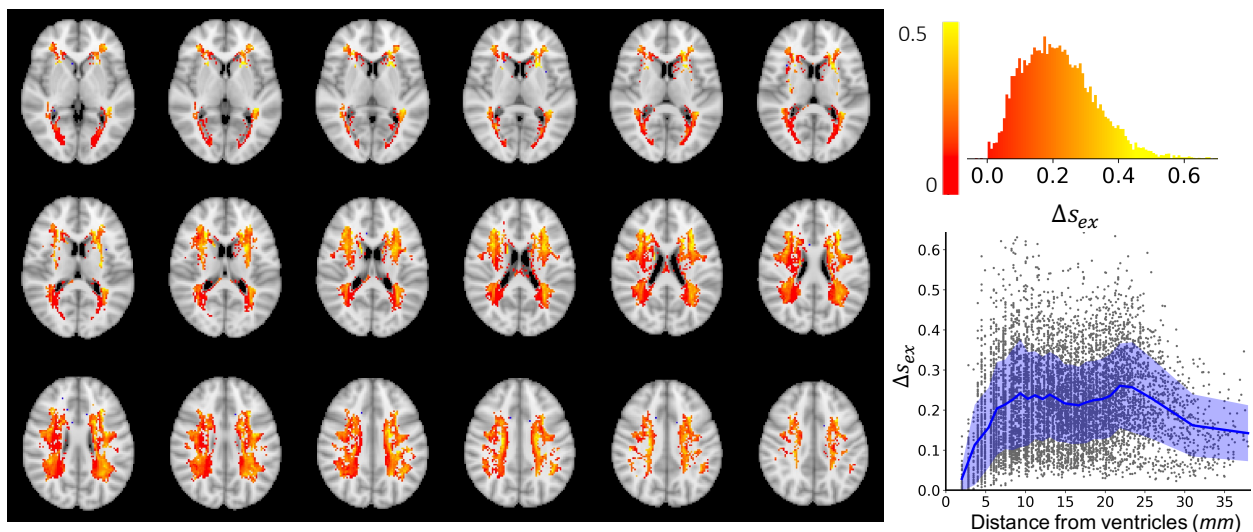


Figure 15. Estimated amount of change in s_{ex} . The maps show the estimated amount of change in s_{ex} in voxels where s_{ex} was the best model using a maximum a posteriori estimation $\Delta s_{ex} = \underset{\Delta v}{\operatorname{argmax}} P(\Delta v \mid y, \Delta y, \hat{\Delta s}_{ex})$. At most of the voxels the estimated amount of change is positive, meaning that an increase in s_{ex} can explain the change in the summary measurements observed in the WMH voxels. The top right panel shows the distribution of estimated amount of change at the voxels where change in s_{ex} was the best model. Most of the estimated changes are between 0 and 0.4. The bottom right panel shows the amount of change vs the distance (in millimeters) from the ventricles.

410 DISCUSSION

411 We presented a Bayesian framework to directly infer changes in parameters of a biophysical
412 model from observed changes in a set of measurements. We applied the method to microstructural
413 modelling of diffusion MRI, where biophysical models usually require many free parameters and
414 are often degenerate.

415 Comparison with model inversion

416 The traditional approach to overcome these degeneracies is to constrain some of the parameters
417 to biologically plausible values so that other parameters can be estimated using a conventional
418 measurement (e.g., fixing the diffusivities in NODDI, (Zhang et al. 2012)). Such assumptions
419 reduce the full model parameter space to a restricted subspace, where the model is invertible. This
420 direct inversion approach has the advantage that it gives parameter estimates and that it can model
421 any parameter change in this restricted subspace. However, violation of these assumptions can
422 significantly bias the parameter estimates.

423 Our proposed approach allows the initial set of parameters to lie anywhere within the full model
424 parameter space (restricted only by broad user-defined priors); and any of these parameters might
425 change. This extra flexibility comes at the price that the parameter changes are assumed to lie along
426 1D lines in parameter space defined by the user-provided patterns of change $\hat{\Delta}v$. For each of these
427 hypothesized 1D change models, we estimate the posterior probability of such a change as well as
428 the most likely amount given the baseline data and the change in it.

429 To compare this assumption with that made by direct inversion, let us consider a biophysical
430 model with 8 free parameters. Let us further assume that, due to the limited degrees of freedom
431 in our model, we can only fit 3 out of these 8 parameters. In this case direct inversion would
432 require assuming that the microstructural change is limited to a subset of three parameters, i.e., a
433 3-dimensional subspace of the full 8-dimensional parameter space. In contrast, BENCH assumes
434 by default that the change is caused by one out of the 8 parameters, which corresponds to the
435 microstructural change lying in one of 8 one-dimensional lines in parameter space. This suggests
436 that if one has prior knowledge of which microstructural parameters are likely to change, it might

437 make sense to use direct inversion with those parameters as free parameters. BENCH would have
438 the advantage in a more exploratory approach, where any of the underlying parameters might have
439 changed. However note that this comparison between approaches is complicated by the fact that
440 using model inversion requires setting a subset of the parameters to some fixed value, which might
441 cause a bias in the free parameters if inaccurately fixed (Jelescu et al. 2016; Novikov et al. 2019b).

442 It is important to note that the user-defined prior distributions for parameters do not directly
443 imply a prior value for the parameters. These priors are used to train the regression models and
444 are required to be wide enough to capture all possible underlying parameter settings. Nevertheless,
445 using broader priors only requires more complex machine learning models that can capture the
446 variation in the relation between the measurements and their derivatives.

447 In the proposed approach we train the models with simulated data once (without requiring any
448 real data) and use the trained models to estimate the desired probabilities for any real data with the
449 same acquisition protocol. This precomputation saves one from having to integrate over all possible
450 initial parameters when inferring the parameter change in each voxel. Therefore, the inference on
451 real data which only consist of a few 1d integrations for each voxel, runs much faster than the
452 non-linear optimizations in alternative inversion approaches.

453 The results from simulations suggest that we are able to identify changes in signal fraction
454 accurately for the given brain-like measurement. However, there is a considerable confusion in the
455 diffusivities, meaning that the change in these parameters is not distinguishable from one another.
456 These accuracy values depend on the baseline measurements, underlying parameters, and the nature
457 of how each parameter affects the measurements. Nevertheless, an important point is even in the
458 case of full confusion in diffusivities, the results from the proposed approach is more reliable
459 compared to the model inversion with fixed parameters. That is because a wrong prior for the fixed
460 parameters can bias the estimates for other parameters, while in the proposed approach we avoid
461 such assumptions. For example, in NODDI we assume the B0 signal is fixed before and after a
462 change (as a result of the sum constraint on the signal fractions), but in our approach we allow the
463 B0 signal also to change arbitrarily.

464 The fact that the approach doesn't require the models to be invertible makes it applicable to
465 studying changes in over-parameterised models or models without closed form analytical solution,
466 e.g. simulation-based models. Such simulation-based models provide the opportunity to explore
467 more complex and realistic models of diffusion in a tissue. There is no limitation in the number of
468 parameters as long as they affect the observed data in some way. If several parameters cause the
469 data to change in the same (or very similar way), this approach will give a list of possible parameters
470 underlying the observed change with a probability associated with each. The resulting probability
471 estimates can be used to eliminate unlikely change scenarios.

472 We utilized the trained models of change for the parameters of the "standard" model for diffusion
473 to investigate which microstructural changes can explain white matter hyperintensities. The results
474 suggest that the change can be associated with an increase in the extracellular signal. This is in
475 line with other findings using more complex diffusion encodings (Lampinen et al. 2019), who
476 found an increase in the extracellular T2, which would lead to an increase in the extracellular
477 signal contribution. Comparing with the inversion approach, here we did not assume diffusivities
478 are fixed in various brain regions, but we assumed only one of the parameters has changed as a
479 result of white matter hyperintensity. However, it is possible that simultaneous changes in multiple
480 parameters can better explain the change in the data, which could be tested in the same framework
481 with the extended models of change. For example, a model with combination of the parameters
482 might be able to explain a positive change in $b0_mean$ and a negative change in $b2_mean$ as it was
483 observed in some voxels.

484 **Summary measures**

485 The choice of summary measurements to train change models is arbitrary, but this choice can
486 affect the performance of the model. It is essential that the summary measurements are able to
487 capture enough information from the data such that they are sensitive to changes in the parameters
488 of interest and insensitive to other changes that are not part of the model parameters. For example,
489 in our simulations we did not include the fibre orientation parameters as part of the free parameters,
490 and therefore we required the summary measures to be rotationally invariant. Hence the choice

491 of decomposing the signals in each shell into spherical harmonics to extract rotationally invariant
492 summary measurements. Of course one can instead use other signal representations, such as
493 measures derived from the diffusion tensor model, or the kurtosis tensor model, etc, to compute
494 the summary measurements. We chose spherical harmonics over other choices as they are fast to
495 calculate, and the bases are orthogonal which leads to summary measures that capture different
496 aspects of the data.

497 **Future developments**

498 While in the examples shown here these patterns of change only altered a single parameter at a
499 time, in the current framework the pattern of change can be any vector in parameter space. In the
500 future we plan to extend this framework to allow for parameter changes in 2D or 3D hyperplanes
501 rather than just along 1D lines. However, the dimensionality of these hyperplanes will always be
502 lower than that of the restricted parameter subspace in which parameters can freely change with the
503 direct inversion approach. Note that computing posterior probabilities in a full Bayesian framework
504 allows for comparison between models of change with different complexities without the need for
505 arbitrary regularisation.

506 In addition, the model of change can be extended to study continuous changes (e.g. ageing), as
507 opposed to discrete group differences as shown in this work. To do so, one first needs to compute the
508 gradient of change in the measurements with respect to the independent variable, e.g. time, using a
509 regression model. Then one can use the chain rule to relate the rate of change in the measurements
510 to the rate of change in the parameters. Such an approach makes modelling continuous change a
511 straightforward extension of this framework.

512 Although here we mostly show how our method can be applied to detect changes in parameters
513 given the data, our framework can also be used to optimize data acquisition protocols for detecting
514 changes in particular parameters of interest. For example, in the simulations we show that it is
515 difficult to detect a change in the free-diffusion parameter. Our framework can be used to extend
516 the acquisition (e.g. by adding lower b-values) and, using the output confusion matrices, establish
517 an optimal set of b-shells to enable detection of change in free diffusion.

518 Finally, while we applied the framework to the specific problem of studying microstructural
519 changes using diffusion MRI in the brain, the framework is general and can be applied in any field
520 where biophysical models are available. For example, the same approach as described in this paper
521 can be applied to dynamical causal models (DCM) (Friston et al. 2003) for fMRI or MEG/EEG.
522 These are notoriously over-parameterised, but often, are applied in a context where the values
523 of the inferred parameters is of lesser interest than the change in the parameters under different
524 experimental conditions; the ideal scenario for BENCH.

525 SOFTWARE

526 BENCH is an open source software implemented in python and available at <https://git.fmrrib.ox.ac.uk/hosseini/bench>.

528 ACKNOWLEDGEMENTS

529 SJ is supported by a Wellcome Senior Fellowship (221933/Z/20/Z), MC and SJ by a Wellcome
530 Collaborative Award (215573/Z/19/Z). The Wellcome Centre for Integrative Neuroimaging is
531 supported by core funding from the Wellcome Trust (203139/Z/16/Z). LG is supported by the
532 National Institute for Health Research (NIHR) Oxford Health Biomedical Research Centre (BRC).
533 UK Biobank Resource under Application 8107 is used in this research. We are grateful to UK
534 Biobank for making the data available, and to all the participants, who made this resource possible
535 by donating their time. The computations were carried out using the Oxford Biomedical Research
536 Computing (BMRC) facilities; a joint development between the Wellcome Centre for Human
537 Genetics and the Big Data Institute that is supported by Health Data Research UK and the NIHR
538 Oxford Biomedical Research Centre. We additionally thank Amy Howard, Paul McCarthy, Mark
539 Woolrich, Karla Miller, Mauro Zucchelli, and Markus Nilsson for their helpful discussions.

540 **REFERENCES**

- 541 Alfaro-Almagro, F., Jenkinson, M., Bangerter, N. K., Andersson, J. L., Griffanti, L., Douaud,
542 G., Sotiropoulos, S. N., Jbabdi, S., Hernandez-Fernandez, M., Vallee, E., et al. (2018). “Image
543 processing and quality control for the first 10,000 brain imaging datasets from uk biobank.”
544 *Neuroimage*, 166, 400–424.
- 545 Andersson, J. L., Jenkinson, M., and Smith, S. (2019). “High resolution nonlinear registration with
546 simultaneous modelling of intensities.” *BioRxiv*, 646802.
- 547 Assaf, Y., Blumenfeld-Katzir, T., Yovel, Y., and Basser, P. J. (2008). “Axc caliber: a method for
548 measuring axon diameter distribution from diffusion mri.” *Magnetic Resonance in Medicine:
549 An Official Journal of the International Society for Magnetic Resonance in Medicine*, 59(6),
550 1347–1354.
- 551 Basser, P. J., Mattiello, J., and LeBihan, D. (1994). “Estimation of the effective self-diffusion tensor
552 from the nmr spin echo.” *Journal of Magnetic Resonance, Series B*, 103(3), 247–254.
- 553 Debbete, S. and Markus, H. (2010). “The clinical importance of white matter hyperintensities on
554 brain magnetic resonance imaging: systematic review and meta-analysis.” *Bmj*, 341.
- 555 Friston, K. J., Harrison, L., and Penny, W. (2003). “Dynamic causal modelling.” *Neuroimage*,
556 19(4), 1273–1302.
- 557 Griffanti, L., Zamboni, G., Khan, A., Li, L., Bonifacio, G., Sundaresan, V., Schulz, U. G., Kuker,
558 W., Battaglini, M., Rothwell, P. M., and Jenkinson, M. (2016). “BIANCA (Brain Intensity
559 AbNormality Classification Algorithm): A new tool for automated segmentation of white matter
560 hyperintensities.” *NeuroImage*, 141, 191–205.
- 561 Jelescu, I. O., Veraart, J., Fieremans, E., and Novikov, D. S. (2016). “Degeneracy in model parameter
562 estimation for multi-compartmental diffusion in neuronal tissue.” *NMR in biomedicine*, 29(1),
563 33.
- 564 Jensen, J. H., Helpert, J. A., Ramani, A., Lu, H., and Kaczynski, K. (2005). “Diffusional kurtosis
565 imaging: the quantification of non-gaussian water diffusion by means of magnetic resonance
566 imaging.” *Magnetic Resonance in Medicine: An Official Journal of the International Society for*

- 567 *Magnetic Resonance in Medicine*, 53(6), 1432–1440.
- 568 Kazhdan, M., Funkhouser, T., and Rusinkiewicz, S. (2003). “Rotation invariant spherical harmonic
569 representation of 3 d shape descriptors.” *Symposium on geometry processing*, Vol. 6, 156–164.
- 570 Lampinen, B., Szczepankiewicz, F., Novén, M., van Westen, D., Hansson, O., Englund, E.,
571 Mårtensson, J., Westin, C.-F., and Nilsson, M. (2019). “Searching for the neurite density with
572 diffusion mri: Challenges for biophysical modeling.” *Human brain mapping*, 40(8), 2529–2545.
- 573 Miller, K. L., Alfaro-Almagro, F., Bangerter, N. K., Thomas, D. L., Yacoub, E., Xu, J., Bartsch,
574 A. J., Jbabdi, S., Sotiropoulos, S. N., Andersson, J. L. R., Griffanti, L., Douaud, G., Okell, T. W.,
575 Weale, P., Dragonu, I., Garratt, S., Hudson, S., Collins, R., Jenkinson, M., Matthews, P. M.,
576 and Smith, S. M. (2016). “Multimodal population brain imaging in the UK Biobank prospective
577 epidemiological study.” *Nature Neuroscience*, 19(11), 1523–1536.
- 578 Novikov, D. S., Fieremans, E., Jespersen, S. N., and Kiselev, V. G. (2019a). “Quantifying brain
579 microstructure with diffusion MRI: Theory and parameter estimation.” *NMR in Biomedicine*,
580 32(4) Publisher: John Wiley & Sons, Ltd.
- 581 Novikov, D. S., Fieremans, E., Jespersen, S. N., and Kiselev, V. G. (2019b). “Quantifying brain
582 microstructure with diffusion mri: Theory and parameter estimation.” *NMR in Biomedicine*,
583 32(4), e3998.
- 584 Novikova, D. S., Veraarta, J., Ileana O. Jelescu, and and Els Fieremans (2018). “Rotationally-
585 invariant mapping of scalar and orientational metrics of neuronal microstructure with diffusion
586 MRI.” *NeuroImage*, 174, 518–538.
- 587 Prins, N. D. and Scheltens, P. (2015). “White matter hyperintensities, cognitive impairment and
588 dementia: an update.” *Nature Reviews Neurology*, 11(3), 157–165.
- 589 Reisert, M., Kellner, E., and Kiselev, V. G. (2017). “Disentangling micro from mesostructure by
590 diffusion MRI: A Bayesian approach.” *NeuroImage*, 147, 964–975 Publisher: Academic Press.
- 591 Sotiropoulos, S. N., Behrens, T. E., and Jbabdi, S. (2012). “Ball and rackets: inferring fiber fanning
592 from diffusion-weighted mri.” *Neuroimage*, 60(2), 1412–1425.
- 593 Virtanen, P., Gommers, R., Oliphant, T. E., Haberland, M., Reddy, T., Cournapeau, D., Burovski, E.,

- 594 Peterson, P., Weckesser, W., Bright, J., van der Walt, S. J., Brett, M., Wilson, J., Millman, K. J.,
595 Mayorov, N., Nelson, A. R. J., Jones, E., Kern, R., Larson, E., Carey, C. J., Polat, İ., Feng, Y.,
596 Moore, E. W., VanderPlas, J., Laxalde, D., Perktold, J., Cimrman, R., Henriksen, I., Quintero,
597 E. A., Harris, C. R., Archibald, A. M., Ribeiro, A. H., Pedregosa, F., van Mulbregt, P., and
598 SciPy 1.0 Contributors (2020). “SciPy 1.0: Fundamental Algorithms for Scientific Computing
599 in Python.” *Nature Methods*, 17, 261–272.
- 600 Wardlaw, J. M., Smith, E. E., Biessels, G. J., Cordonnier, C., Fazekas, F., Frayne, R., Lindley,
601 R. I., T O’Brien, J., Barkhof, F., Benavente, O. R., et al. (2013). “Neuroimaging standards for
602 research into small vessel disease and its contribution to ageing and neurodegeneration.” *The
603 Lancet Neurology*, 12(8), 822–838.
- 604 Woolrich, M. W., Jbabdi, S., Patenaude, B., Chappell, M., Makni, S., Behrens, T., Beckmann,
605 C., Jenkinson, M., and Smith, S. M. (2009). “Bayesian analysis of neuroimaging data in fsl.”
606 *Neuroimage*, 45(1), S173–S186.
- 607 Zhang, H., Schneider, T., Wheeler-Kingshott, C. A., and Alexander, D. C. (2012). “NODDI: Practi-
608 cal in vivo neurite orientation dispersion and density imaging of the human brain.” *NeuroImage*,
609 61(4), 1000–1016.
- 610 Zhang, Y., Brady, J. M., and Smith, S. (2000). “Hidden markov random field model for segmentation
611 of brain mr image.” *Medical Imaging 2000: Image Processing*, Vol. 3979, International Society
612 for Optics and Photonics, 1126–1137.
- 613 Zucchelli, M., Deslauriers-Gauthier, S., and Deriche, R. (2020). “A computational Framework
614 for generating rotation invariant features and its application in diffusion MRI.” *Medical Image
615 Analysis*, 60, 101597.